Title	A through-process, thermomechanical model for predicting welding-induced microstructure evolution and post-weld high-temperature fatigue response
Author(s)	Mac Ardghail, Padraig; Harrison, Noel M.; Leen, Sean B.
Publication Date	2018-02-11
Publication Information	Mac Ardghail, P., Harrison, N., & Leen, S. B. (2018). A through-process, thermomechanical model for predicting welding-induced microstructure evolution and post-weld high-temperature fatigue response. International Journal of Fatigue, 112, 216-232. doi: https://doi.org/10.1016/j.ijfatigue.2018.02.015
Publisher	Elsevier
Link to publisher's version	https://doi.org/10.1016/j.ijfatigue.2018.02.015
Item record	http://hdl.handle.net/10379/15596
DOI	http://dx.doi.org/10.1016/j.ijfatigue.2018.02.015

A through-process, thermomechanical model for predicting welding-induced microstructure evolution and post-weld high-temperature fatigue response

P Mac Ardghail[1, 2], N. Harrison[1, 2], S. B. Leen[1, 2]

[1]Mechanical Engineering, College of Engineering and Informatics, NUI Galway, University Road, Galway, Ireland.

[2]Ryan Institute for Environmental, Marine and Energy Research, NUI Galway, University Road, Galway, Ireland.

Contact : p.macardghail1@nuigalway.ie, +353 87 213 8818

ABSTRACT: This paper is concerned with the development of a modelling framework to predict the effects of welding and post-weld heat treatment on thermo-mechanical performance of welded material, as a step towards a design tool for industry. A dislocation mechanics, through-process finite element model, incorporating thermal, microstructural and mechanical effects is presented, for predicting thermo-mechanical fatigue of welds. The model is applied to multi-pass gas tungsten arc welding of 9Cr martensitic steel. The predicted high-temperature low-cycle fatigue performance of cross-weld samples is comparatively assessed for a range of different post-weld heat treatment durations. It is shown that longer post-weld heat-treatment (PWHT) durations increase the predicted number of cycles to failure and that Vickers hardness gradient across the heat-affected zone can be used an indicator of fatigue life.

KEY WORDS: Finite-element, welding, fatigue, microstructure, constitutive

1 INTRODUCTION

The secure generation of clean and sustainable electricity is a major challenge facing Ireland, the EU and the world. Thermal power plant has traditionally operated under base-load (constant output) conditions. Current and next generation power plant is required to increasingly operate alongside renewable energy sources, such as wind energy, in order to reduce carbon emissions according to the European Commission [1]. However, renewable energy sources can be intermittent and unpredictable and energy storage remains a challenge. Thermal power plant must operate more flexibly to compensate for inconsistent renewable energy output, an operating condition known as 'load-following'.

Load-following operation will increase thermo-mechanical fatigue (TMF) and high-temperature low cycle fatigue (HTLCF) on power plant components, often made from 9Cr steels, and cause early failure via cyclic softening and microstructure degradation, as shown by Sauzay et al.[2]. Therefore design for thermal fatigue of next-generation weldments is critically important.

9Cr steels are high-temperature, martensitic steels with carbide precipitate nano-strengthening. These steels perform well at high temperature due to their hierarchical microstructure, which consists of prior-austenite grains (PAGs), within which are packets. Each packet consists of blocks, which consist of high dislocation-density martensitic laths. Dispersed randomly throughout each lath are fine MX precipitates and solutes comprised of single elements, while larger $M_{23}C_6$ carbides disperse along lath and PAG boundaries, as shown by the works of Sauzay [2], Hurtado-Norena [3] and Ennis [4], among others.

The strength of 9Cr steels come from their high dislocation-density. Materials soften as dislocation-density decreases, such as when dislocations move, meet and annihilate each other. 9Cr steels maintain dislocation-density at high temperatures, and thus strength, because the microstructure retards dislocation motion. The PAG and packet boundaries are difficult

for dislocations to cross and the carbides and precipitates are relatively immobile and hence cause pinning of dislocations, as shown by Sauzay et al.[2]. Current in-service 9Cr material was designed before the increased use of load-following operation, which introduces additional cyclic strains and dislocation motion, leading to premature softening and failure of components.

The parent material (PM) microstructure is achieved via carefully-controlled heat-treatment processes to deliver optimum performance at high temperature. Welding causes local high temperatures and heating rates which compromise the original PM microstructure. This compromised region is known as the heat-affected zone (HAZ). The HAZ is sub-divided into separate regions known as coarse-grained HAZ, fine-grained HAZ and inter-critical HAZ (CGHAZ, FGHAZ, ICHAZ). CGHAZ is located closest to the weld filler metal in a joint, ICHAZ is located closest to the PM and FGHAZ is in between.

Type IV cracking failure of plant components occurs in the ICHAZ. Most work on Type IV cracking has focused on creep-dominated failure but high-temperature fatigue produces similar failure, according to Farragher et al.[5].

One solution to this problem is to design a new material where the HAZ microstructure is similar to that of PM. This has been achieved by, for example, the addition of boron and a new candidate material, MarBN, is currently under review by Abe and co-workers[6, 7]. However, power plant operators can be slow to adopt new materials for multiple reasons, including the development of new industry codes and standards as well as confidence in long-term performance of welded assemblies. Therefore, improving the welding process for better performance of current 9Cr steels is an attractive proposition.

This work presents a through-process modelling methodology for simulation of welding and in-service operation of 9Cr steel components. The through-process methodology is implemented in three stages.

Firstly, a thermal model simulates the heat transfer and temperature histories experienced by a component during welding. Secondly, a microstructural model uses the temperature histories from the thermal simulation to predict the evolution of salient hierarchical microstructure parameters (viz. phase volume fractions, prior austenite grain size, lath width and hardness). Thirdly, a dislocation-mechanics-based constitutive model is used in a sequentially-coupled thermo-mechanical analysis to predict the constitutive response of the material during and after welding, incorporating the effects of welding-induced microstructure evolution. Previous work by the authors focused only on phases volume fractions, either just within the ICHAZ [8], or within a cross-weld (CW) specimen [9]. This work expands upon those works by incorporating more microstructural parameters, which lead to a more sophisticated constitutive model.

The constitutive models for individual phases are calibrated using published P92 data by Yaghi et al. [10] for tempered and untempered martensite and austenite. The resulting mixed-phase response for the different welded regions (e.g. ICHAZ) are compared against published data by Touboul et al. [11] obtained using digital image correlation for welded P91.

2 METHODOLOGY

2.1 Welding process model

A transient thermal model for multi-pass gas tungsten arc welding (GTAW) was developed, following the methodology of Yaghi et al. [12]. The finite-element (FE) code Abaqus/Standard was adopted here. An element-birth method is used to activate mesh regions corresponding to individual weld beads. Figure 1 shows sample temperature contour distributions for an axisymmetric 36-pass model, for different numbers of completed passes.

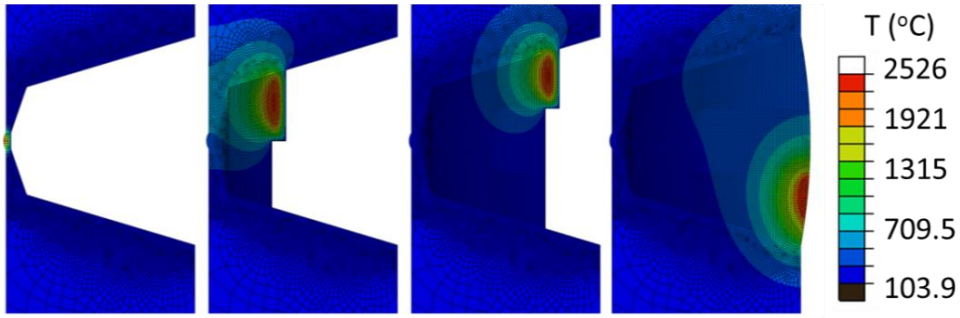

(a) (b) (c) (d)

Fig. 1. Thermal contour plots for a 36-pass welding simulation for the (a) 1st pass, (b) 9th pass, (c) 22nd pass and (d) 36th pass.

A similar principle is used for the geometry in the present work. The sequential thermo-mechanical analysis incorporates a special-purpose Abaqus user-material (UMAT) subroutine, developed here to compute solid-state phase evolution based on temperature history and the phase equilibrium diagram. The solid-state phases considered in this work are austenite (γ) and martensite (α'). Volume-fraction evolution for austenite, V_γ, is defined with a linear lever rule:

$$V_\gamma = 1 - \frac{A_{c3} - T}{A_{c3} - A_{c1}} \quad (1)$$

where A_{c3} (924°C) is the finish temperature for austenite transformation, A_{c1} (830°C) is the start temperature for austenite transformation and T is the current temperature. The values of A_{c1} and A_{c3} were obtained from Yaghi et al. [10]. For martensitic transformation, the Koistinen-Marburger (K-M) function [13], was used as follows:

$$V_{\alpha'} = \lambda\left(1 - \exp\left[-0.011\left(M_S - T\right)\right]\right) \quad (2)$$

where M_s (400°C) is the martensite transformation start temperature according to the continuous cooling transformation (CCT) diagram, from the steel manufacturer Vallourec [14], and T is current temperature. λ is a constant used to ensure that martensite volume

fraction reaches a value of 1 by the time the material reaches 100°C, the martensitic transformation finish temperature, M_f. In this work, it is assumed that only austenite exists at high temperatures and only martensite exists at low temperatures, as implied by the CCT diagram and by the phase equilibrium diagram from Cerjak et al. [15] for 9Cr steels. For simplicity, and due to the high delta-ferrite start temperature of around 1200°C [15], the present work does not simulate the formation of delta-ferrite. The solidus and liquidus temperatures are obtained from the literature [12] and are taken as 1450°C and 1500°C, respectively.

Metallurgical strain, caused when volume increase caused by martensitic transformation counteracts thermal contraction during cooling, as described by Francis et al. [16], was modelled via the following equation [10]:

$$\Delta\varepsilon_{MET} = \lambda_2 \Delta T \exp\left[-0.011(M_s - T)\right] \quad (3)$$

where λ_2 is a constant and ΔT is the incremental change in temperature.

2.2 Microstructure evolution model

The modelling methodology is physically-based, with dependence on microstructural features, including martensitic lath width and prior-austenite grain size. A microstructure evolution model is implemented in this work. Heat-treatment data from Potirniche et al. [17] was used to calibrate a Vickers hardness model to predict softening during tempering and hardening during normalizing of 9Cr steel:

$$\dot{H} = -\left(g\left(H - H_f\right) + k\right) \quad (4)$$

where H is the room-temperature Vickers hardness, g and k are temperature-dependent parameters and H_f is an asymptotic hardness towards which the value of H trends:

$$g = 1.15 \times 10^{-6} T - 4.97 \times 10^{-4} \quad (5)$$

$$k = 4.6036\times10^{-3} - 5.6\times10^{-6}T \quad (6)$$

$$H_f = 832.45 - 0.8091T \quad (7)$$

After H approximately reaches H_f, further linear softening is assumed to occur:

$$\dot{H} = -k \quad (8)$$

The Vickers hardness can increase during normalising according to:

$$\dot{H} = 7g\left(H_m - H\right) \quad (9)$$

where H_m is asymptotic hardness:

$$H_m = 1000 - H_f \quad (10)$$

Calibration of the hardness model (Eqn. 4 to 7) is displayed in Figure 2.

Data from Ennis and Czyrska-Filemonowisc [4] and Milovic et al. [18] was used to predict prior-austenite grain growth as a function of time and temperature. An initial PAG size of 50 microns was assumed for this work. PAG size evolution focuses on recrystallization and growth. Recystallisation is defined by a recrystallized volume fraction, S, according to:

$$\dot{S} = \phi_1\left(1 - S\right) \quad (11)$$

where ϕ_1 is a temperature-dependent parameter. Simulated-welding test data [18] showed a reduction in grain size for temperatures up to 950°C. These tests allowed inference of recrystallised volume fraction from the reduction in grain-size; for example, it was assumed that a 25% reduction in grain size corresponded to a 25% recrystallised volume fraction, viz. S-value of 0.25. The recrystallized volume fraction evolution controls grain size, d, according to:

$$\dot{d} = \frac{\phi_2}{d} - \phi_3\dot{S} \quad (12)$$

where ϕ_2 is a temperature-dependent parameters and ϕ_3 is a constant. The second term in Eqn. 12 relates recrystallized volume fraction to grain size, based on the data [18]. For grain growth after recrystallization, data accounting for rapid grain growth at high temperature [18]

and more gradual grain growth with saturation values at different temperatures [4], was employed. Equations 11 and 12 are simplified versions of recrystallization and grain growth equations used by Li et al. [19]. The calibration of this model is described in Fig. 3.

Heat treatment, microstructural and mechanical data from Barbadikar et al. [20] was used in conjunction with the hardness model to devise an empirical heat-treatment-microstructure model which relates lath-width, L, to hardness, H, and prior-austenite grain size, d:

$$L = \mu_1 + \mu_2 d - (\mu_3 + \mu_4 d)H \tag{13}$$

where μ_1, μ_2, μ_3 and μ_4 are temperature-independent constants. The result of this relationship is displayed in Fig. 4.

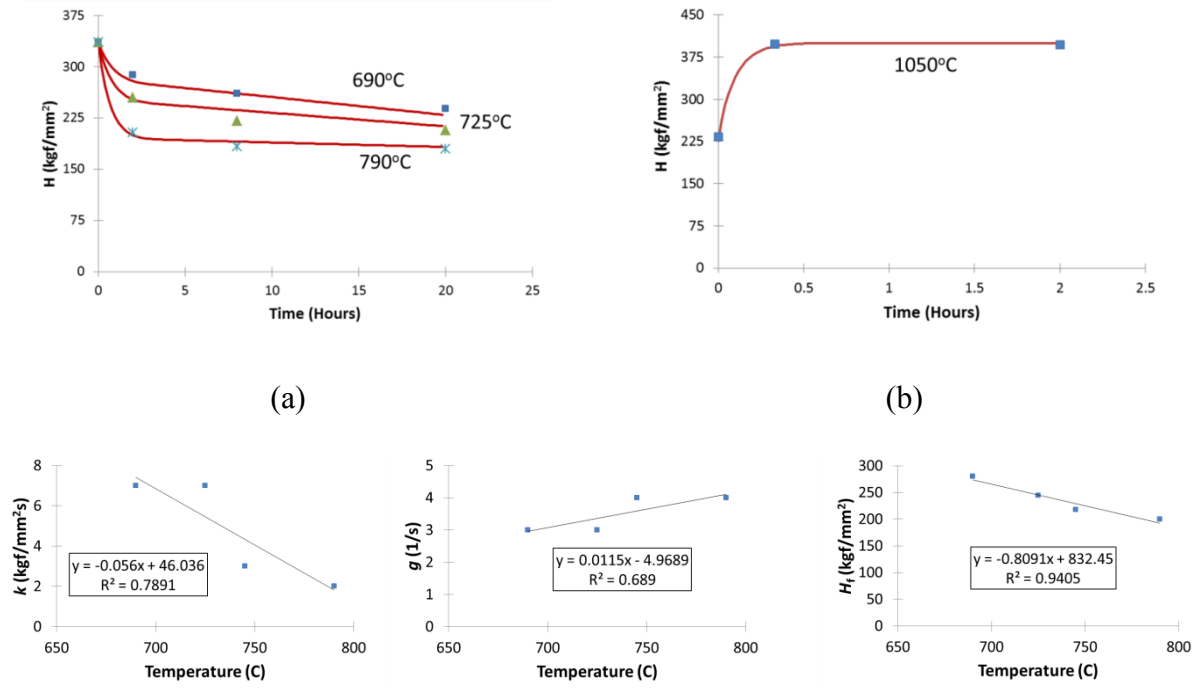

Fig. 2. Calibration of the hardness evolution model showing (a) a sample plot of the model (lines) versus data from Potirniche et al. [17](points) at different tempering temperatures, (b) a sample plot of

increasing hardness after normalising, and identification of (c) the softening parameter k, (d) the tempering softening rate variable, g, and (e) the asymptotic tempering hardness, H_f.

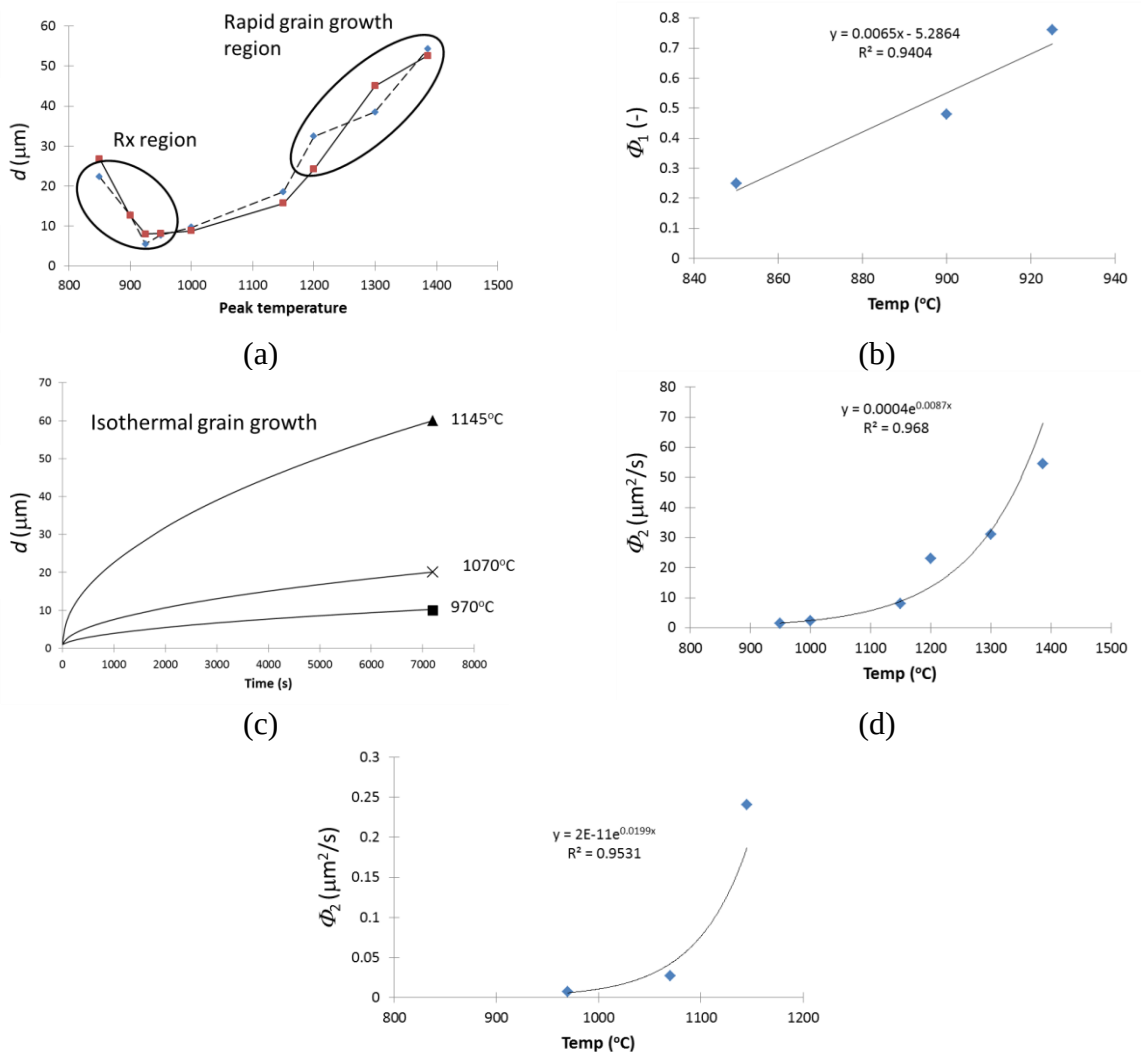

Fig. 3. Calibration of the PAG size evolution model showing (a) a plot of the model (dashed lines) versus data from Milovic et al. [18] (solid lines), (b) the identification of the recrystallization parameter φ_1, (c) a plot of the model (lines) versus data from Ennis et al. [4] (points), (d) the rapid grain growth identification of φ_2 for thermally transient conditions and (e) the grain growth identification of φ_2 for isothermal conditions.

The primary variable controlling the lath width is the hardness, which varies during both welding and PWHT, while PAG size only changes during welding in this work. Hardness evolution also occurs over a wider temperature range than PAG size evolution, making its contribution to lath size greater over the course of the simulation.

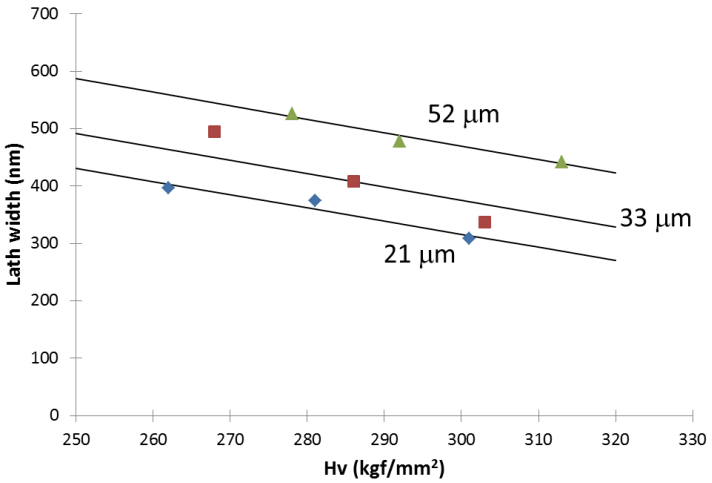

Fig. 4. The relationship between Vickers hardness, prior austenite grain size and lath width, based on data from Barbadikar et al. [20].

2.3 Constitutive model with damage

The microstructure evolution due to the thermo-mechanical history of the GTAW process influences the post-weld mechanical behaviour. A unified viscoplastic, dislocation-density based material model is therefore developed here to capture the temperature-dependent material response of the various heat-affect zones, for both the welding and post-welding response, and is implemented in multiaxial form within the UMAT mentioned above. The uniaxial form is presented here, for conciseness. A hyperbolic sine flow-rule is implemented as follows:

$$\dot{\varepsilon}_p = \alpha \sinh\left(\beta\left(\frac{|\sigma-\chi|}{(1-D)}-\sigma_y\right)\right) \tag{14}$$

where α and β are temperature-dependent variables. Elasticity is defined via Hooke's law as:

$$\dot{\sigma} = E\left(\dot{\varepsilon} - \dot{\varepsilon}_p\right) \tag{15}$$

The kinematic hardening variable, χ, is defined in terms of a Taylor-like hardening dislocation density model as:

$$\dot{\chi} = \frac{B\dot{\bar{\rho}}_r}{\sqrt{\bar{\rho}_r}} \tag{16}$$

where B is:

$$B = \frac{\alpha_g MG\sqrt{b}}{\sqrt{L}} \tag{17}$$

and α_g is a multiplicative constant, M is Taylor factor and b is magnitude of Burgers vector. Note that it is assumed here that the lath width, L, is the mean dislocation free path length, as described by Wei et al. [21]. G is shear modulus and a Poisson's ratio of 0.3 was assumed. Equation 4 uses dislocation density, normalized here as $\bar{\rho} = 1 - \rho_i / \rho$, where ρ is current dislocation density and ρ_i is initial dislocation density for an unstrained material, or a material not experiencing plastic deformation, as used by Li et al. [19]. Dislocation density accumulation (e.g. due to Frank-Read sources) during plastic deformation is defined as:

$$\dot{\bar{\rho}} = c_1\left(1 - \bar{\rho}\right)\left|\dot{\varepsilon}_p\right| \tag{18}$$

Dislocation density evolution typically includes recovery processes, such as annihilation, locking, etc., as well as accumulation to give a combined dislocation density evolution term as follows:

$$\dot{\bar{\rho}}_r = \dot{\bar{\rho}} - c_2\bar{\rho} \tag{19}$$

Physically, $\bar{\rho}_r$ represents the dislocation density at a grain or lath boundary, where recovery occurs. Equation 18 does not include recovery and represents the dislocations which move from the middle of laths towards the boundaries.

The damage term, D, in Equation 14 represents the presence of cracks and voids, which reduce the load-bearing area of a component. This process is described schematically in Fig. 4. The explicit form of damage as a function of dislocation density is as follows:

$$D = a_1\left(1-\frac{\left(\bar{\rho}_r/\bar{\rho}\right)}{y_1}\right)^{x_1} + a_2\left(1-\frac{\left(\bar{\rho}_r/\bar{\rho}\right)}{y_2}\right)^{x_2} \tag{20}$$

where y_1 and y_2 represent critical ratios of the dislocation densities. Both $\bar{\rho}$ and $\bar{\rho}_r$ are assumed to contribute to damage evolution. The mechanism is described in Fig. 5.

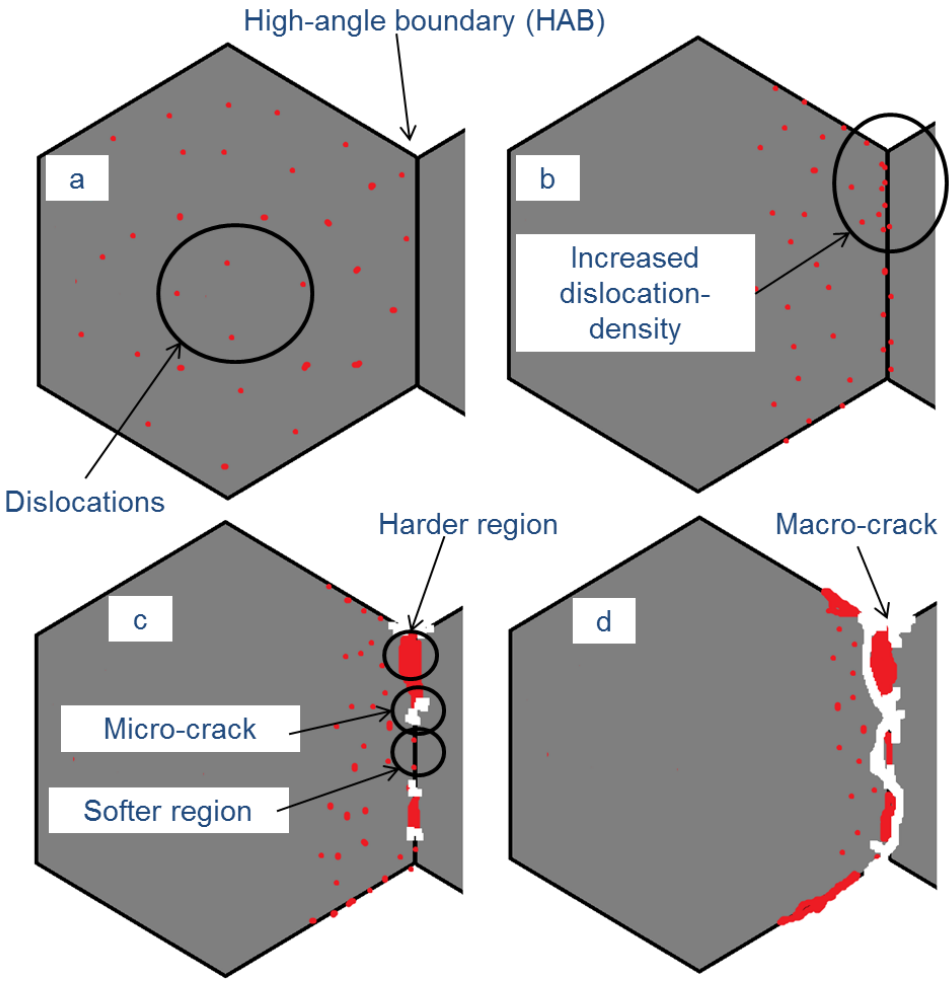

Fig. 5. A schematic representation of the dislocation-density-driven damage model from (a) as-received, unstrained material, (b) deformed material with increased dislocation-density, (c) hard-soft region incompatibility and micro-cracks, (d) failure.

In Fig. 5a, the material is unstrained with some initial dislocation density so both $\bar{\rho}$ and $\bar{\rho}_r$ are zero. As the material strains, Fig. 5b, the dislocation density increases. It is assumed that, as the bulk $\bar{\rho} - \bar{\rho}_r$ increases, local dislocation-density heterogeneities increase too. Some regions will experience greater dislocation-density recovery than others, leading to some regions with higher local dislocation-densities, e.g. $\bar{\rho}$, and other regions with lower dislocation-densities, e.g. $\bar{\rho}_r$. Regions with higher local dislocation-densities will be harder than regions of lower dislocation density and the hard-soft interfaces between local regions will cause strain incompatibilities and create micro-cracks, Fig. 5c, as represented by the first term on the right-hand side of Eqn. 20. As this process continues, Fig. 5d, the micro-cracks grow and join together, leading to macro-void formation and rapid failure, as simulated by the second term on the right-hand side of Eqn. 20.

The modelling parameters for Eqns. 14 to 20 were identified in a step-by-step process, using the temperature-dependent tensile stress-strain dataset shown in Fig. 5, for tempered and untempered martensite and austenite [10]. For the tempered and untempered martensite, the microstructural model described above, together with heat-treatment data [10], allows prediction of lath widths and hence constitutive parameters and mechanical behavior for either condition of martensite material (Fig. 6a, Fig. 6b). For dual-phase (mixed austenite and martensite) regions, a rule-of-mixtures approach was adopted wherein the volume fraction of each phase was used as a weighted average to determine the mixed-phase constitutive parameter value from the individual martensite (tempered or untampered) and austenite values.

Each set of parameter values was obtained separately. First, the visco-plastic parameters α and β were identified from monotonic test data at a single strain-rate 0.001/s [10]. The process is described in Fig. 7:

1. Data from the stress-strain curve (pre-ultimate tensile stress, Fig. 7a) is used to deduce plastic strain-rate and the value of the yield criterion, *f*, where $f = \frac{|\sigma - \chi|}{1-D} - \sigma_y$, following the equation $\dot{\varepsilon}_p = \alpha \sinh(\beta f)$ (Fig. 7b).

2. The monotonic data is used to predict the *f*-value corresponding to the total strain-rate, in this case 0.001/s (Fig. 7c). This provides one coordinate for fitting α and β and the origin is another point.

3. At the flow-stress, the plastic strain rate is approximately equal to the total strain rate and the f-value is related to the Young's modulus, $f \approx E\Delta\varepsilon \approx E\Delta\varepsilon_p \approx E\dot{\varepsilon}_p\Delta t$ (Fig. 7d). For a small strain-rate, the time increment was assumed to be 1s. This provided a third coordinate with which to identify α and β (Fig. 7e, Fig. 7f)

4. Using this method, α and β were identified at each of the relevant temperatures. A uniaxial model was applied to two sets of monotonic test data for P92, one at 20^{o}C and another at 650^{o}C (Fig. 7g). The data came from [10] and [22]. At 20^{o}C, there was no apparent strain-rate effect, as expected, but at 650^{o}C, there was a strain-rate effect and the model successfully predicted the strain-rate effect. The authors took this result as justification for assuming a time increment of 1s when determining the *f*-value at low strain-rates.

Then, for each temperature in turn, the parameter c_1 was identified to capture the initial hardening, immediately post-yield, low strain region of the stress-strain curves (as shown in Fig 8, for example, for a temperature of 20^{o}C); then, the parameter c_2 was identified from the post-yield, moderate strain (but pre-UTS) region (as also shown in Fig. 8) to reduce the hardening rate as strain increased. At high temperatures, the parameter c_2 controlled the flow stress.

From the true stress-strain curve, damage could be identified as a function of strain, enabling fitting of the damage parameters a_1, x_1 and y_1, with a_2, x_2 and y_2 fitted to provide

final failure. The first term in Eqn. 20, using parameters a_1, x_1 and y_1, corresponds to the 'damage region' Fig. 8 and the second term in Eqn. 20 corresponds to the 'failure region' in Fig. 8. The values of these parameters for untempered martensite, tempered martensite and austenite are displayed in Tables 1 to 7.

In Fig. 6c, it appears as though the austenite suffers little or no damage at 400°C or 850°C but does at 650°C. This presents limitations to the austenite damage parameters but the authors do not consider this to be detrimental to the material model. At high temperatures, the material is expected to be too soft to suffer damage. At temperatures below 400°C, the austenite will begin to transform to martensite and adopt martensite damage parameters. The austenite is not expected to persist for long enough between 850°C and 400°C to suffer significant damage, if any.

To account for temperature-dependence, the modelling parameters at different temperatures were described using double-sigmoidal equations, to account for values rising and falling with temperature. A double-sigmoidal function provided a better fit to the parameter values than linear or exponential functions. Some parameters were found to be temperature independent (Table 7). For martensite, the parameters controlling the sigmoidal formulation were linearly related to predicted lath widths. The complete set of results for the individual phase calibrations is displayed in Fig. 6.

Table 1. Temperature-dependent untempered martensite constitutive parameters.

T (°C)	E (GPa)	σ_y (MPa)	c_1 (-)	c_2 (1/s)
20	215	1170	0.25	0.045
200	207	1080	0.4	0.03
400	198	954	0.5	0.03
550	156	900	0.4	0.04
650	114	475	0.05	0.1
850	40.2	88	0.001	0.1

Table 2. Temperature-dependent tempered martensite constitutive parameters.

T (°C)	E (GPa)	σ_y (MPa)	c_1 (-)	c_2 (1/s)
20	215	600	0.25	0.01
200	207	550	0.25	0.015
400	198	490	0.25	0.015
550	156	406	0.15	0.02
650	114	300	0.04	0.1
850	40.2	82	0.01	0.1

Table 3. Temperature-dependent austenite constitutive parameters.

T (°C)	E (GPa)	σ_y (MPa)	c_1 (-)	c_2 (1/s)
400	198	140	0.08	0
650	114	110	0.15	0.002
850	40.2	94	0.1	0.02

Table 4. Temperature-dependent untempered martensite damage parameters.

T (°C)	a_1(-)	x_1(-)	y_1(-)	y_2(-)
20	1.25	2.5	0.41	0.22
200	1.5	2.5	0.347	0.258
400	3	2	0.315	0.25
550	1.5	3	0.612	0.281
650	0.3	2.5	0.785	0.077
850	1.5	2.25	0.05	0.029

2.4 Fatigue response

Attention is focused here on strain-controlled, low cycle fatigue response. Kinematic hardening is adopted due to (i) the possibility of thermo-mechanical cycling during the multi-pass welding process and (ii) the cyclic plasticity nature of the post-weld HTLCF tests used for validation. Tensile test data has been employed here, as a starting point, due to unavailability of comprehensive strain-controlled, cyclic test data for the three different phases (tempered, untempered martensite, austenite) at the multiple different temperatures, strain-rates and strain-ranges. Therefore, in this work, we have assumed that the phase-dependent, temperature-dependent hardening parameters can be identified from the isothermal, monotonic stress-strain responses of the individual phases across the relevant range of temperatures.

The behaviour model for the fatigue response consists of a number of different aspects covering (i) cyclic evolution of yield stress, (ii) cyclic evolution of dislocation density, and (iii) cyclic evolution of dislocation-based damage. (ii) and (iii) are defined to be plastic strain and temperature dependent. The fatigue model assumes that within each cycle, tensile damage still accrues, whilst cyclic damage accrues from cycle to cycle.

It is well known that 9Cr steels experience rapid early cyclic softening, e.g.[23]; this is modelled here as a cyclic decrease in yield stress, as follows:

$$\frac{d\sigma_y}{dN} = -a_3\left(\sigma_y + \sigma_{y\min}\right) \tag{21}$$

σ_{ymin} is a temperature-dependent parameter towards which σ_y converges, thus serving a similar purpose to the cyclic softening parameter used by Barrett et al. [24].

Table 5. Temperature-dependent tempered martensite damage parameters.

T (ºC)	a_1(-)	x_1(-)	y_1(-)	y_2(-)
20	3.5	2	0.67	0.49
200	2.2	2	0.646	0.426
400	2.5	2	0.62	0.424
550	2.5	3.5	0.674	0.24
650	1.2	17	0.76	0.04
850	1.2	2	0.06	0.03

Table 6. Temperature-dependent austenite damage parameters.

T (ºC)	a_1(-)	x_1(-)	y_1(-)	y_2(-)
400	0	1.4	0.1	0
650	25	1.4	0.81	0
850	0	1.4	0.1	0

Table 7. Temperature-independent damage parameters.

Material	a_2(-)	x_2(-)
Untempered martensite	10	1.3
Tempered martensite	16	1.25
Austenite	0	0

In Eqns. 18 and 19, normalized dislocation density increases with plastic strain. A similar formulation was used in [19] for large deformation during line pipe fabrication. In this work, the application of Eqns. 18 and 19 was for fully-reversed loading. It was assumed that some dislocations which move towards high-angle boundaries during plastic deformation return along their path and move away from high-angle boundaries during elastic unloading. Thus within each fatigue half-cycle, the dislocation density increases during plastic deformation and reduces during elastic unloading. This reduction was represented as a cyclic change in normalized dislocation density, which was calibrated against data in [23] (Fig. 6a):

$$\frac{d\bar{\rho}}{dN} = \bar{\rho}\left(1-\psi_1\right) \tag{22}$$

$$\psi_1 = k_1 p + k_2 + T\left(k_3 + k_4 p\right) \tag{23}$$

where k_1, k_2, k_3, and k_4 are constants and p is the effective plastic strain experienced from the initial onset of yield until elastic unloading. Different values of ψ_1 were identified for different plastic strain ranges at different temperatures and a bilinear relationship between p and T was used to define Eqn. 21, as shown in Fig. 9. Equation 22 applies to both $\bar{\rho}$ and $\bar{\rho}_r$.

Equation 22 is not a replacement for Eqns. 18 and 19. Within one fatigue half-cycle, Eqns. 18 and 19 is used to define the dislocation-density, hardening and damage. When the material unloads, Eqn. 22 is used to normalise the dislocation density again and this new normalised value will be the initial value of dislocation-density going into the next fatigue half-cycle.

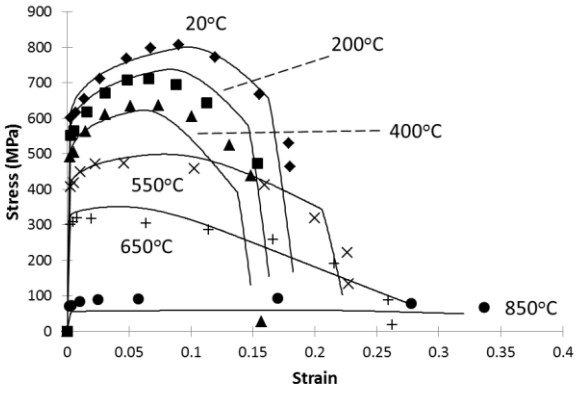

(a)

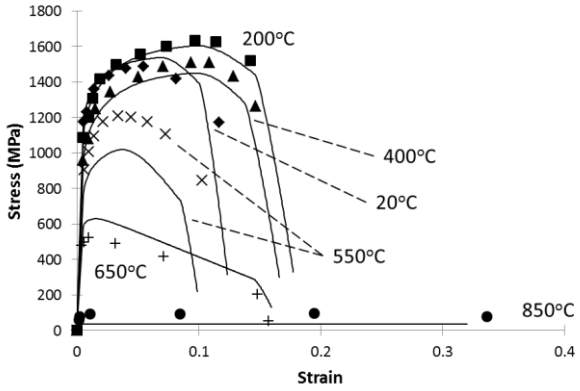

(b)

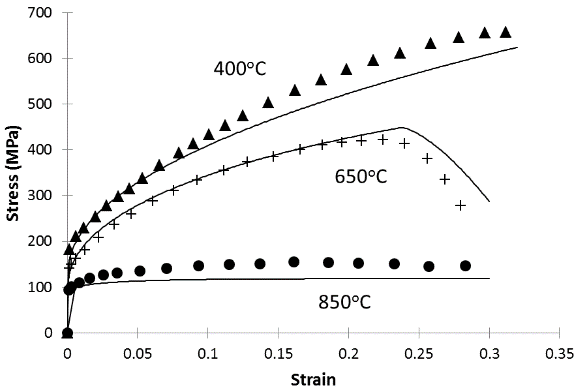

(c)

Fig. 6. Calibration of the material model against (a) tempered martensite, (b) untempered martensite and (c) austenite data at a range of temperatures.

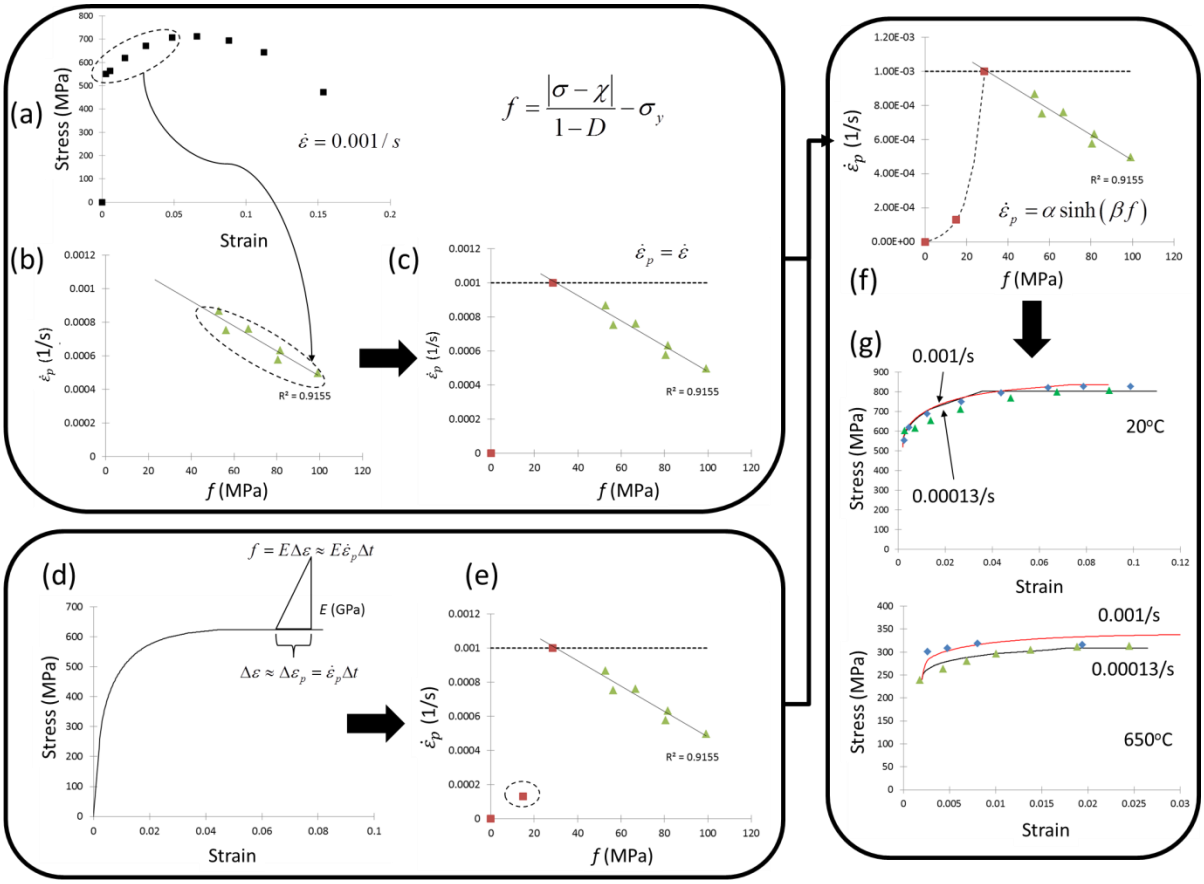

Fig. 7. The identification of the parameters α and β from monotonic data, including the results of the model applied to monotonic data from two sets of tests.

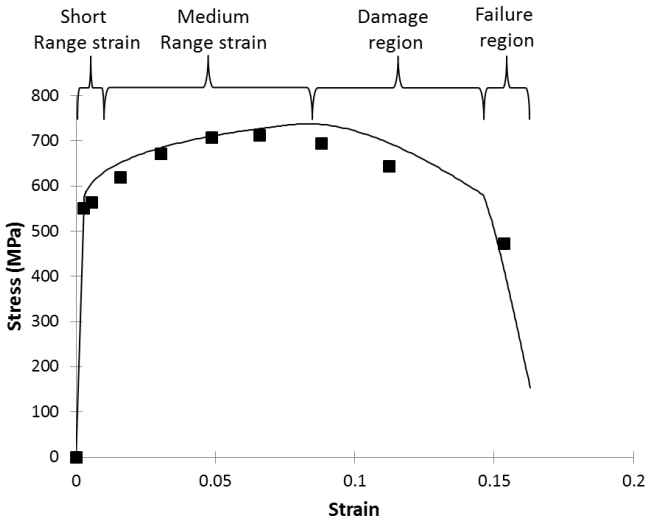

Fig. 8. A schematic of a stress-strain curve showing the parameter-identification portions corresponding to different aspects of the constitutive and damage model.

An additional damage term, D_2, is introduced to produce secondary softening, as follows:

$$D_2 = a_1 \left(1 - \frac{\left(\bar{\rho}_r / \bar{\rho} \right)}{y_3} \right)^{x_2} \tag{24}$$

where a_1 and x_2 are the same as in Eqn. 20. The new parameter y_3 evolves cyclically as follows:

$$\frac{dy_3}{dN} = k_5 p + k_6 + T\left(k_7 + k_8 p\right) \tag{25}$$

where k_5, k_6, k_7, and k_8 are constants. The parameter y_3 starts at a low value and increases cyclically until it reaches the (reducing) dislocation-density ratio, at which point failure is predicted to occur.

Figure 9 shows the identification process of the parameters k_5, k_6, k_7, and k_8 across different temperatures and plastic strains (corresponding to different plastic strain ranges):

1. After the monotonic constitutive model is developed, a uniaxial simulation is conducted. Cyclic softening (Eqn. 21) reduces the peak tensile cyclic stress. The parameter ψ (Eqn. 23) is then fitted to provide secondary softening (dashed line, Fig. 9a).

2. When ψ is fitted, the uniaxial simulation can be repeated to track the evolution of the dislocation-density ratio, $\bar{\rho}_r / \bar{\rho}$ (Fig. 9b). This ratio can be checked when the simulation reaches the number of cycles at which failure occurs, according to test data [23]. This provides y_3 and $\frac{dy_3}{dN}$ values, assuming an initial y_3-value of zero (Fig. 9b).

3. Concurently, the amount of plastic strain, p, in each cycle can be calculated based on the simulation results and an average value taken (Fig. 9c).

4. For a range of strain ranges and temperatures, values of p and $\frac{dy_3}{dN}$ can be identified (Fig. 9d). The linear relationship is of the form $ax + b$, which can then be separated to find the temperature dependence of a (Fig. 9e) and b (Fig. 9f). This process identifies the modelling parameters k_5, k_6, k_7, and k_8.

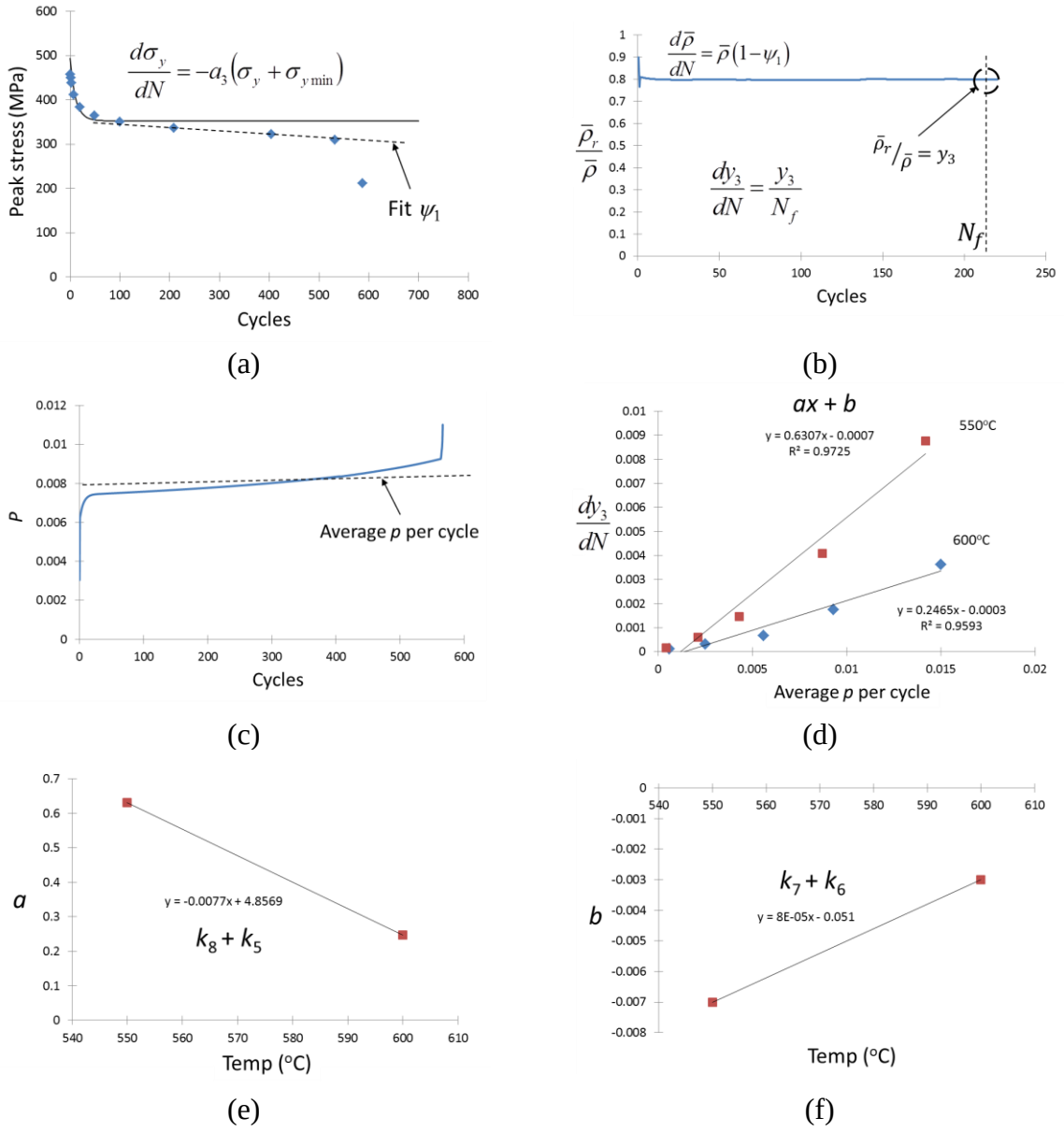

Fig. 9. The identification of the parameters k_5, k_6, k_7, and k_8, based on uniaxial simulations.

Figure 10 describes how eqns. 21 to 25 correspond to different aspects of 9Cr steel cyclic response. Equation 21 corresponds to primary cyclic softening in the first 40 to 50 cycles. Equation 22 was calibrated to provide the secondary softening via Eqn. 20. Equation 25 was calibrated to provide the final cyclic damage described in Eqn. 24.

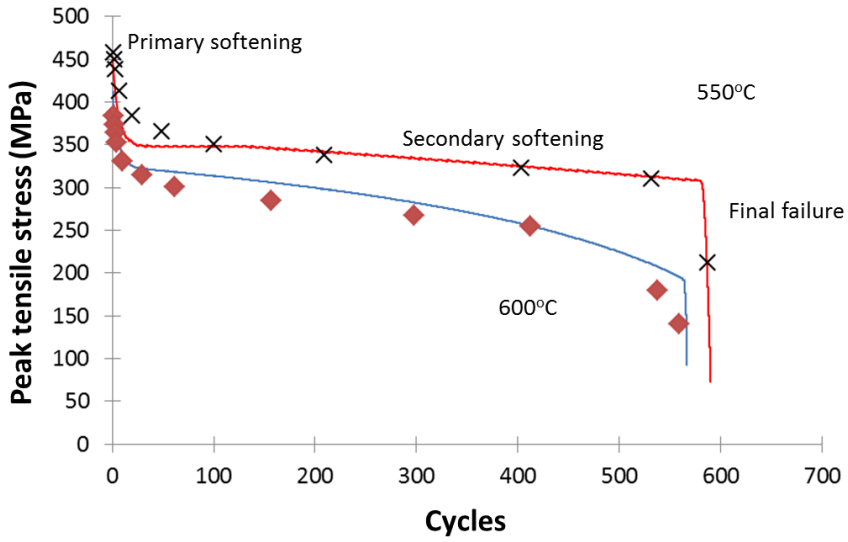

Fig. 10. Results for the calibration of the fatigue model peak stress per cycle (line) against published P91 PM data (points) from Shankar et al [23] at 550°C and 600°C, strain range 1.2% and strain rate 0.3%/s with the primary softening, secondary softening and final failure regions highlighted.

The material model is described in the flowcharts in Figs. 11 to 13. State-dependent variable (SDVs), including damage, dislocation density, microstructure variables, etc., are called from the previous step in the analysis. For the first step, material parameters are initialized. The model reads in thermal data from the results of the thermal simulation and calculates phase volume fraction, hardness and other microstructure evolution. Based on temperature and lath width, constitutive parameters are calculated and combined via a rule-of-mixtures approach for austenite and martensite. A strain increment is applied either due to thermal expansion,

metallurgical strain or applied strain during cyclic loading and the yield criterion is checked. If the material yields, then an implicit, Newton-Raphson iterative solver is applied to calculate the constitutive response. The direction of the loading during yielding for the current step is compared to the direction during the previous step and the cyclic parameters in Eqns. 21 to 25 are updated if the loading direction has changed. Finally Hooke's Law is applied to calculate stress increments for the applied strain increments.

This work focuses on the fatigue response of a cross-weld specimen. The weld metal in the cross-weld specimen was specified as an elastically-perfectly-plastic material. The temperature-dependent Young's modulus for the WM was taken from Yaghi et al. [12].

At high temperatures, above the highest calibration temperature of 850^{o}C, for example, the material is defined as being perfectly plastic. The temperature-dependent Young's modulus decreases with temperature and is defined in the Abaqus UMAT to saturate at 1 GPa.

2.5 FE Simulation

The specimen simulated in this work represents a CW specimen (Fig. 10). An axi-symmetric geometry, radius 3.5 mm and height 20 mm, was created and four weld passes were applied to it. The mesh element types were DAXC8 for thermal analysis and CAX8R for structural analysis.

The axisymmetric geometry was an attractive option for a number of reasons. Firstly, power-plant components are typically pipe sections and tensile-test specimens are typically cylindrical, thus an axisymmetric geometry is consistent with physical specimens. Secondly, axisymmetric models are computationally cheap to use. For example, in the work of Deng et al. [25], a 3D geometry had 9600 elements and 12300 nodes compared to an axisymmetric model with 300 elements and 357 nodes and the residual stress predictions of both models in that work were in good agreement. Thirdly, the predicted results are not expected to be

rendered inaccurate by the use of an axisymmetric model. Both Deng et al.[25] and Dong [26] found that axisymmetric geometries produced residual stress results similar to those of 3D models.

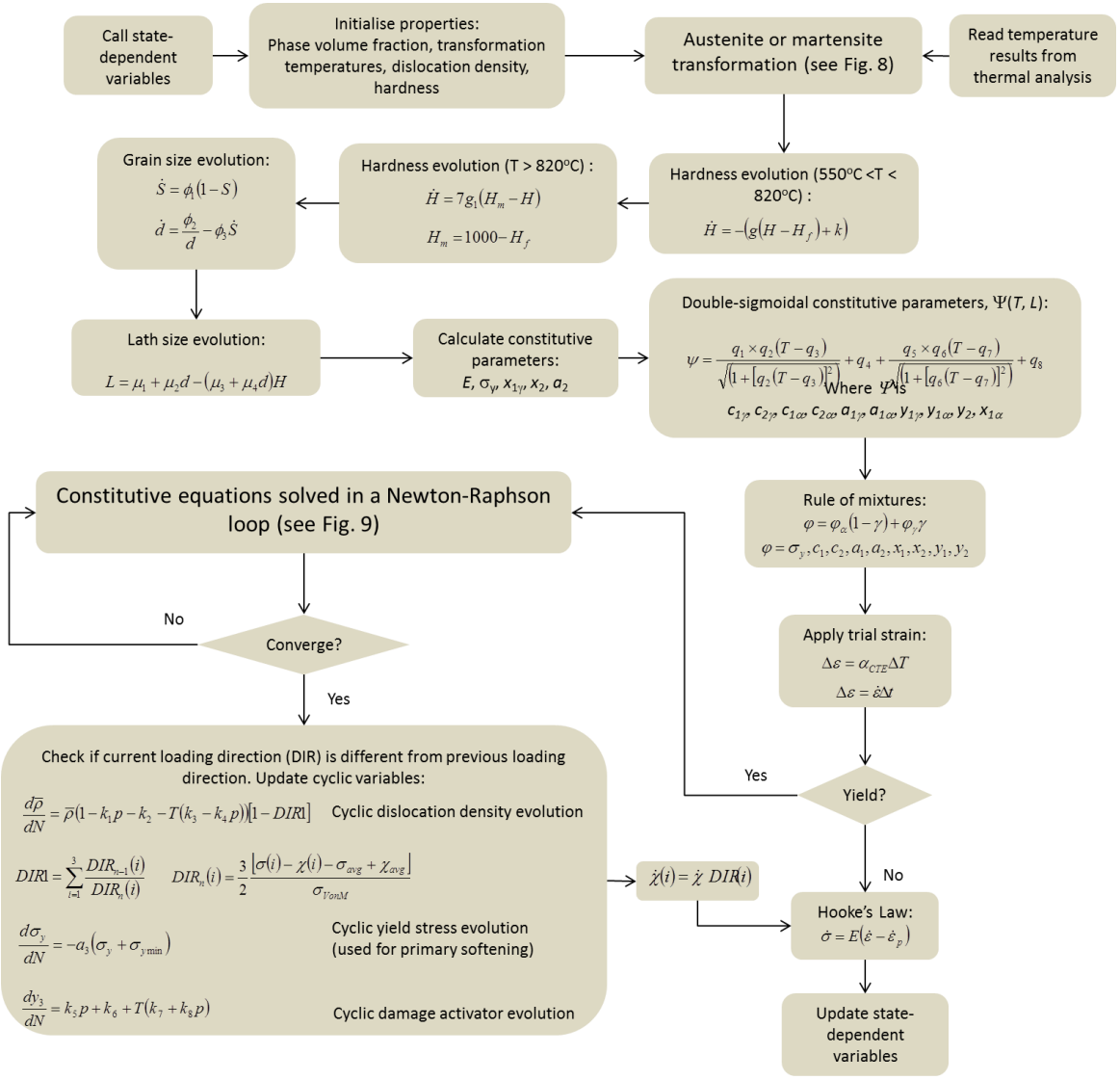

Fig. 11. The user material subroutine's flowchart, from calling state-dependent variables from the previous step, through the microstructure evolution model, the constitutive model and the Newton-Raphson implicit solver and updated SDVs.

The current work uses a method known as block-dumping, where all weld beads are included in the geometry and are activated to represent the laying of the weld bead [27]. The heat was supplied by a temperature boundary condition as this was the most convenient for the purposes of this work, which is to demonstrate a through-process methodology. An alternative method would be to apply a heat load based on welding torch parameters, described as DFLUX in Yaghi et al. [12] but for the purposes of this work, it was considered sufficient to produce weld beads independently of specific weld torch parameters, thus a temperature boundary condition was specified. The axisymmetric model did not lend itself to the use of a moving heat source, such as that proposed by Goldak et al. [28] because the axisymmetric nature of the model geometry applies heat at all points around the circumference of the geometry simulataneously and an axially-moving heat source was not considered in the current work.

Each of the four welding passes involved heating the material to a temperature of 1600^{o}C, exceeding the material melt temperature of 1500^{o}C from Yaghi et al. [12], over a 0.25 s period and holding at that temperature for a further 0.25 s. The inter-pass time was 30 seconds. To expedite the simulation, the material was forcibly cooled to 25^{o}C 30 s after the final weld pass with a 30 s quench at a constant cooling rate, rather than allowing natural cooling. This simplification did not influence the microstructure evolution because the predicted temperature at the start of the quench was low enough that microstructure evolution had already completed.

Post-weld heat treatment (PWHT) was simulated at 750^{o}C for 300 s and 600 s, with 100 s heating and cooling times. The material was then reheated to 600^{o}C and subjected to fully-reversed fatigue loading, with a strain range of 3% and a strain rate of 0.3%. These fatigue loading parameters were selected to ensure failure within relatively few cycles so as to expedite fatigue simulation.

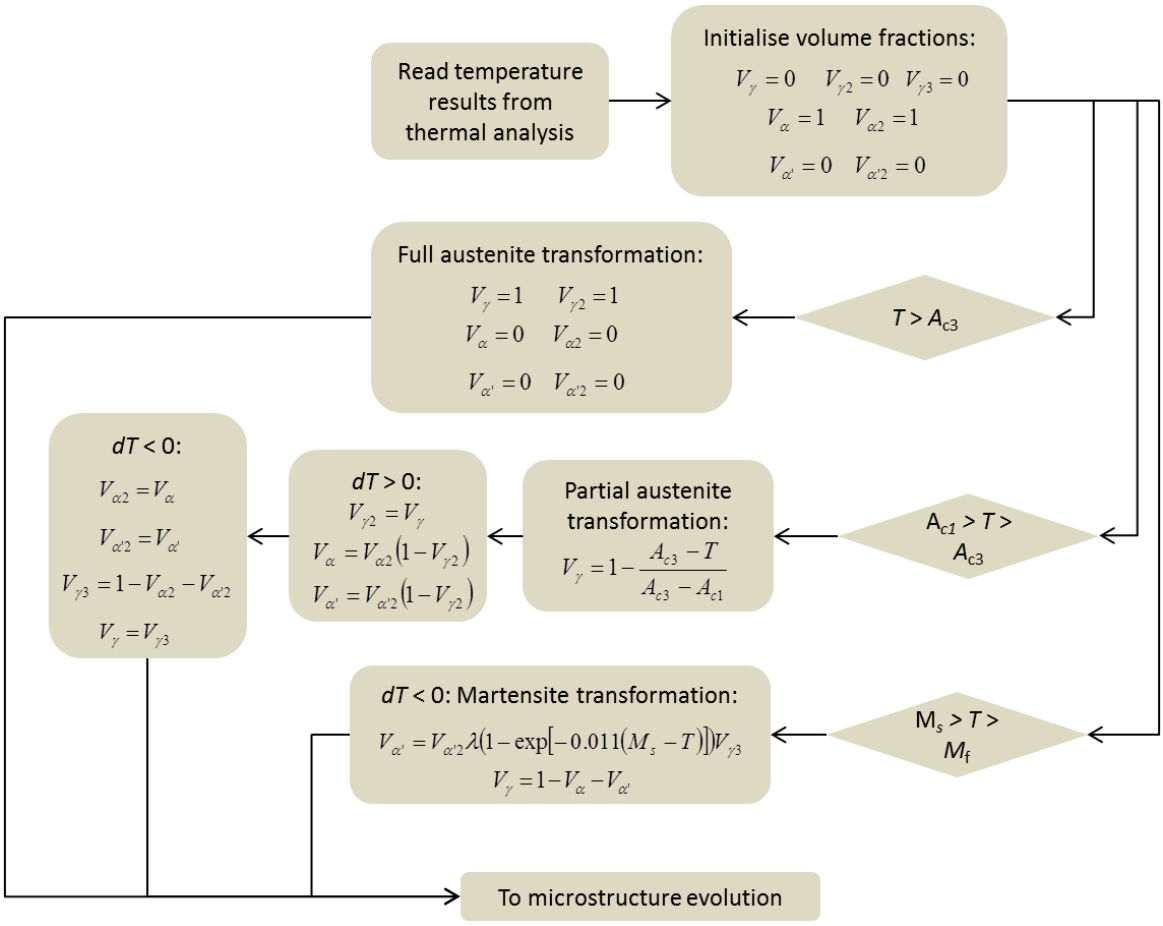

Fig. 12. The user material subroutine's flowchart for solid-state phase volume fraction evolution.

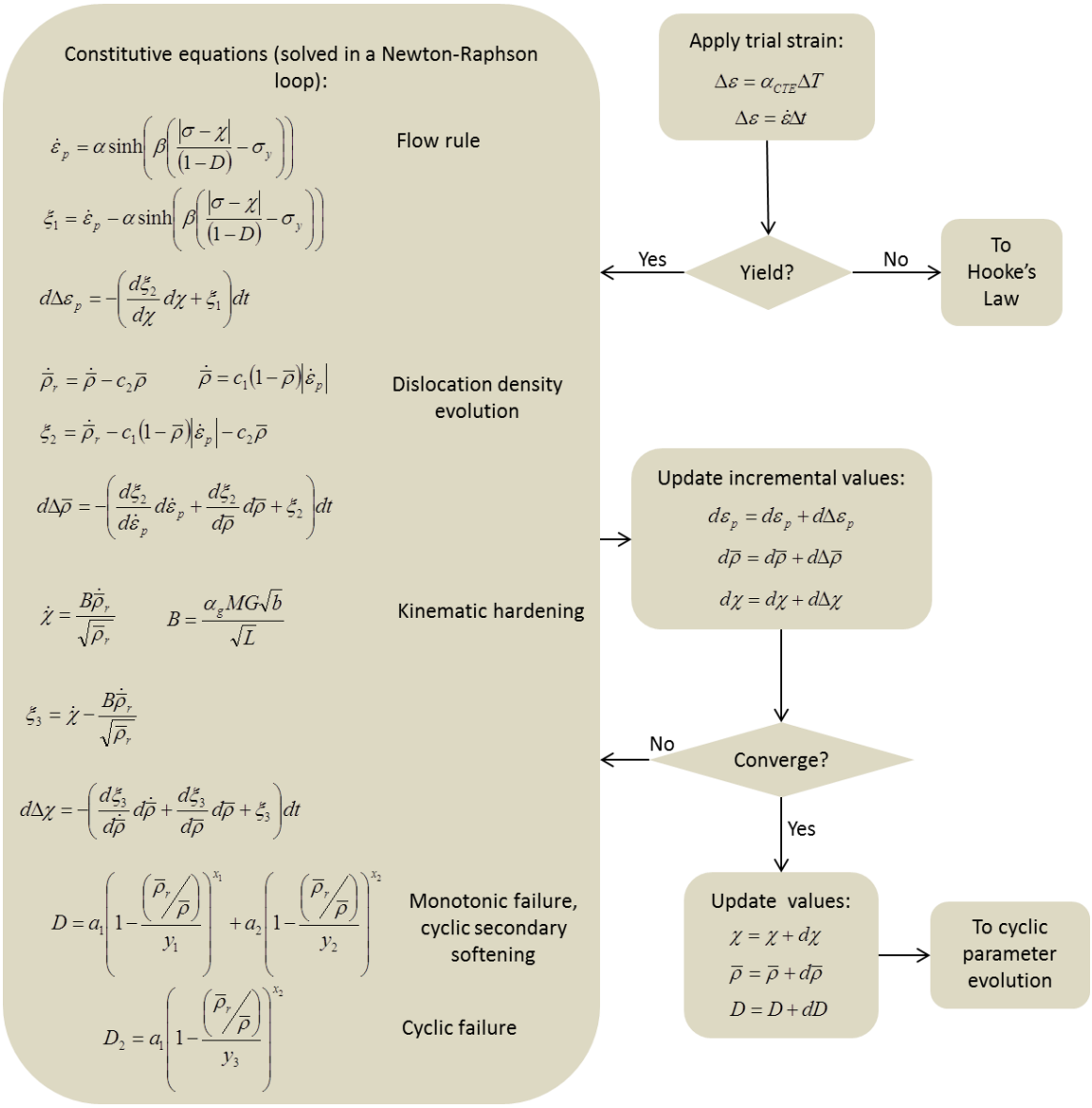

Fig. 13. The user material subroutine's flowchart for implicit Newton-Raphson solver for the constitutive equations.

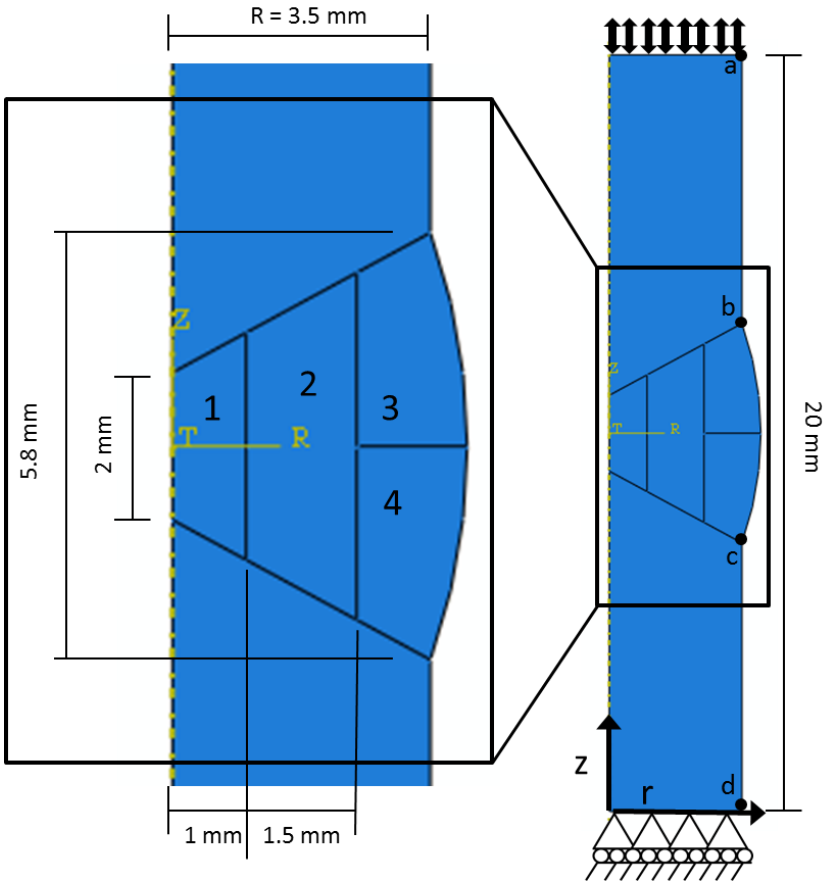

Fig. 14. The axi-symmetric cross-weld simulation geometry used in this work with the weld pass sequence (labelled 1 to 4) and positions a to d on the outside surface.

3 RESULTS

3.1 Constitutive model – validation

Touboul et al. [11] used digital image correlation (DIC) to infer monotonic tensile stress-strain responses for ICHAZ and PM (as well as CGHAZ, FGHAZ and WM) from a P91 cross-weld flat test specimen at room temperature (RT) and at 625^{o}C; relevant microstructure data, viz. hardness and PAG size, was also presented for the various heat-affected regions. The latter data have been used as input to the constitutive model of the present work. A comparison of the resulting RT and 625^{o}C responses is shown in Fig. 15. Note that these model predictions are not based on the through-process model. Rather, an FE geometry was partitioned into separate HAZ regions and prescribed the microstructure properties (hardness,

PAG size) from [11] and the local stress-strain histories were recorded. It is clear that the model predicts the qualitative general trend of lower strength and ductility for the ICHAZ, relative to the PM, for both temperatures.

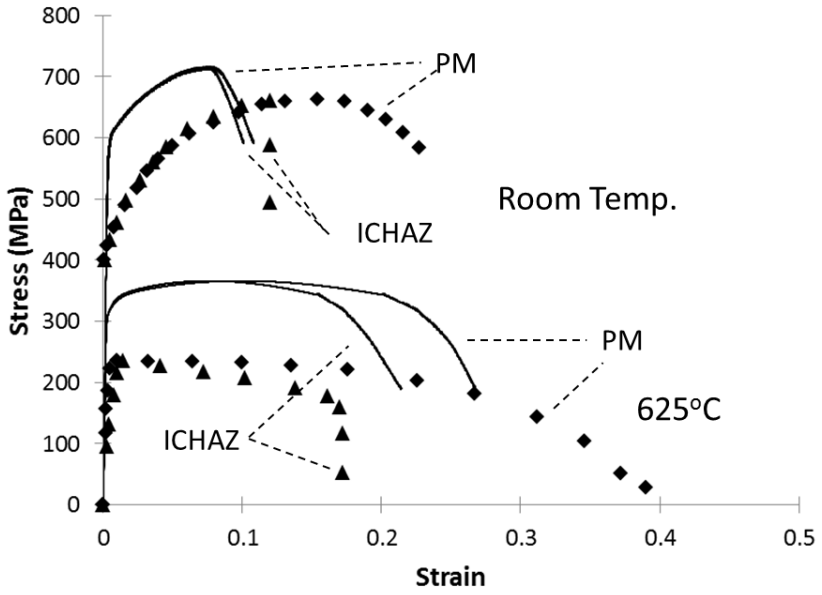

Fig. 15. Comparison of the predicted PM and ICHAZ responses (lines) to DIC measured responses (points) at room temperature and at 625°C.

3.2 Welding microstructure evolution

Figure 16 shows evolution of PAG size during the welding simulation. The HAZ is clearly visible as the region in which the microstructure has been altered from that of the PM. From the evolution of the PAG size, the locations of the ICHAZ, FGHAZ and CGHAZ can be predicted. Microstructure evolution is not simulated in the WM. The initial PAG size was 50 μm and welding led to sizes as small as ~1 μm.

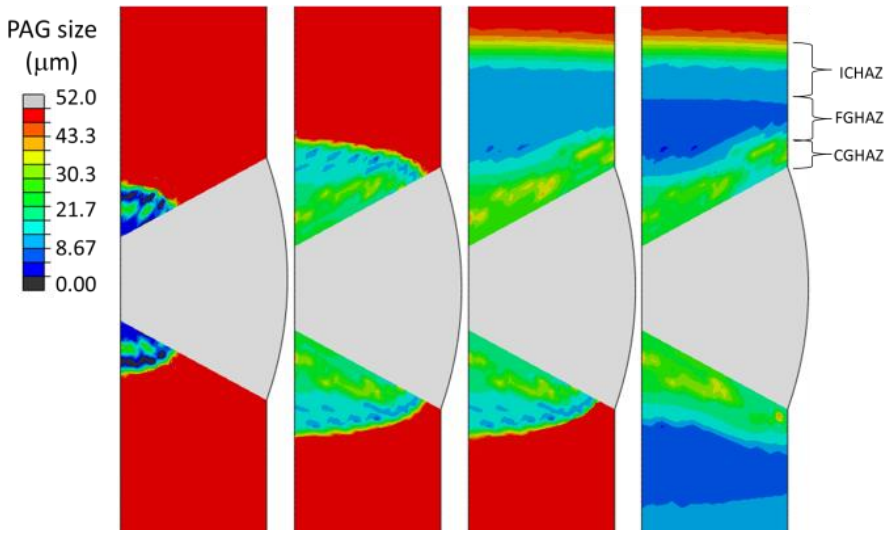

Fig. 16. Predicted prior-austenite grain size contour plots after (a) 1, (b) 2, (c) 3 and (d) 4 passes. Note that WM microstructure evolution is not simulated.

Figure 17 shows the lath width evolution of the material during the welding simulation (initial state, after the second weld pass and after the fourth weld pass) along two discrete paths.

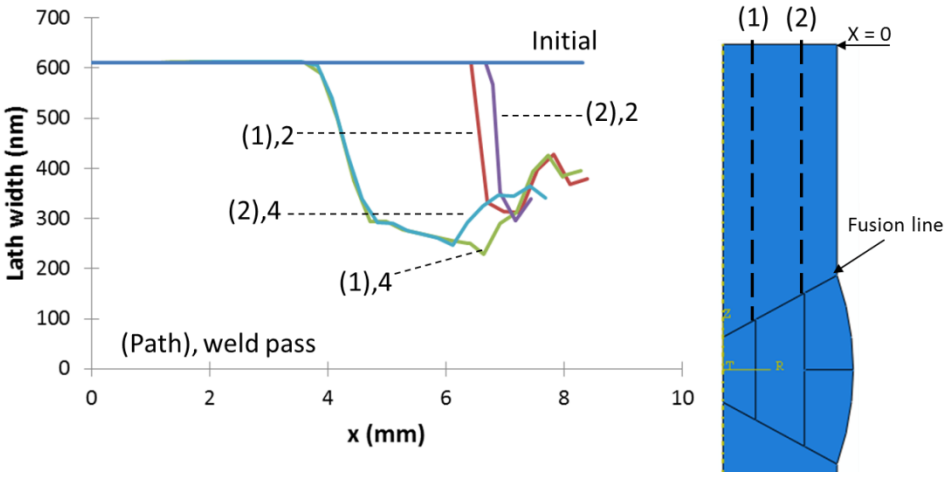

Fig. 17. Predicted lath width contour plots for the initial state, after the second weld pass and after the fourth weld pass along paths (1) and (2) highlighted in the schematic of the geometry.

It can be seen that the lath width reduces significantly after a weld pass, which represents the presence of new, untempered material. Regions close to the fusion line remain hotter for longer than regions further from the fusion line and some lath-coarsening due to auto-tempering is predicted. The majority of this auto-tempering is predicted to occur by the end of the second weld pass and only a slight change is predicted by the end of the fourth pass. Overall, the initial lath width was 611 nm and laths as small as ~220 nm were predicted after welding. After 600s of PWHT, the lath width generally increased and ranged from ~268 nm to 625 nm.

Figure 18 shows the through-process predicted surface hardness distributions for the as-welded (AW) state, as well as after each of the PWHT processes, for the outside surface of the CW specimen, between points a and b in Fig. 14. The model clearly predicts a reduction in hardness distribution with increasing PWHT time. The initial hardness (before welding) was 255 kgf/mm^2; the predicted peak as-welded hardness is ~287 kgf/mm^2, and the predicted peak hardness after 600 s of PWHT is ~275 kgf/mm^2.

3.3 High-temperature, low-cycle fatigue response

Figure 19 shows a sample predicted cyclic response at 600ºC (strain range 2%, strain rate 0.3%/s) for the as-welded specimen. Table 8 shows a comparison of the tests, from Shankar et al. [23], and model-predicted results for CW and PM fatigue lives.

It can be seen in Table 8 that the measured CW lives [23] are lower than those of the PM and that this result is replicated by the model. The model predicts a greater weld life reduction factor (WLRF), $WLRF = \frac{N_f^{PM}}{N_f^{CW}}$, than the test data, apparently due to shorter PWHT times, which were chosen (i) to reduce computation time while still demonstrating the

model's ability to include the effects of PWHT and (ii) because the predicted effects of PWHT appeared to reach a stabilized value within the durations modelled in the present study.

A sensitivity study was conducted for the as-welded cross-weld specimen to examine the separate influences of the hardness evolution model (Eqn. 7) and the PAG size evolution model (Eqns. 11 and 12) on the predicted number of cycles to failure. The predicted life at a 3% strain range was not significantly affected and at lower strain ranges, the predicted as-welded lives for both cases approached those of the test data [23], despite the test data pertaining to post-weld heat treated material. Therefore both hardness and PAG size evolutions must be taken into account for physically-representative fatigue life predictions.

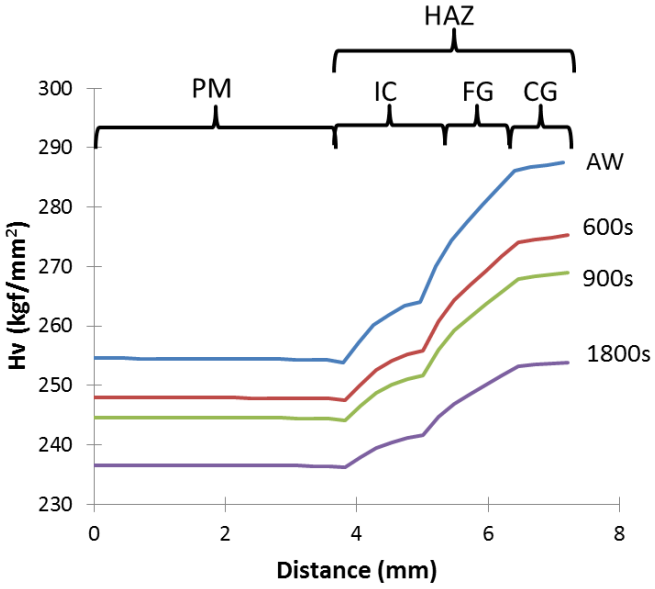

Fig. 18. Post-weld Vickers hardness along the outside surface of the specimen from points a to b (see Fig. 14) for the as-welded (AW) case and for different PWHT times.

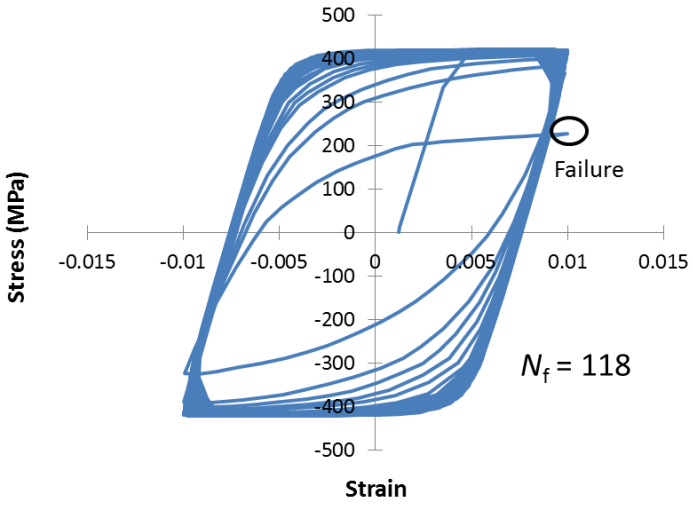

Fig. 19. The predicted stress-strain response for the as-welded case at 600ºC, strain range 2%, strain rate 0.3%/s.

Table 8. Comparison between model and test data [23] cycles to failure at 600ºC, including weld life reduction factor (WLRF)

Data	Strain range (%)	N_f (PM)	N_f (CW)	PWHT (mins)	WLRF
Test	2	287	226	180	1.27
	0.8	1340	1230	180	1.09
	0.5	2690	2250	180	1.20
Model	2	276	118	0 (As-welded)	2.34
			177.5	10	1.55
			187.5	15	1.47
			192	30	1.44
	3	112	71.5	0 (As-welded)	1.57
			72.3	10	1.55
			73	30	1.53

The present through-process model predicts a range of lives for the 2% strain-range CW (depending on PWHT time), from 118 cycles to 192 cycles, all of which are lower than the predicted PM life. It is clear that the largest PWHT prediction gives the closest correlation to the test data (2% range). For the 3% case, the effect of PWHT on improving the WLRF is slight compared to the 2% case. The model predictions presented here capture the detrimental effect of welding on the material response as well as the beneficial effect of PWHT.

Figure 20 shows the damage evolution for the as-welded case. For clarity, the damage contour plot is limited to damage above 0.8, which helps highlight failure regions. The model predicted no damage due to the welding process. Damage was predicted to be negligible until the 78th cycle (Fig. 20a), when a small damaged region was predicted in the FGHAZ. Damage was predicted to evolve rapidly throughout the FGHAZ and ICHAZ until final failure. As expected, little or no damage was predicted for the CGHAZ. Damage nucleation occurred in regions close to where the smallest PAG and lath sizes occurred, e.g. where the material was most brittle. This demonstrates the detrimental effect of untempered martensite on HAZ failure.

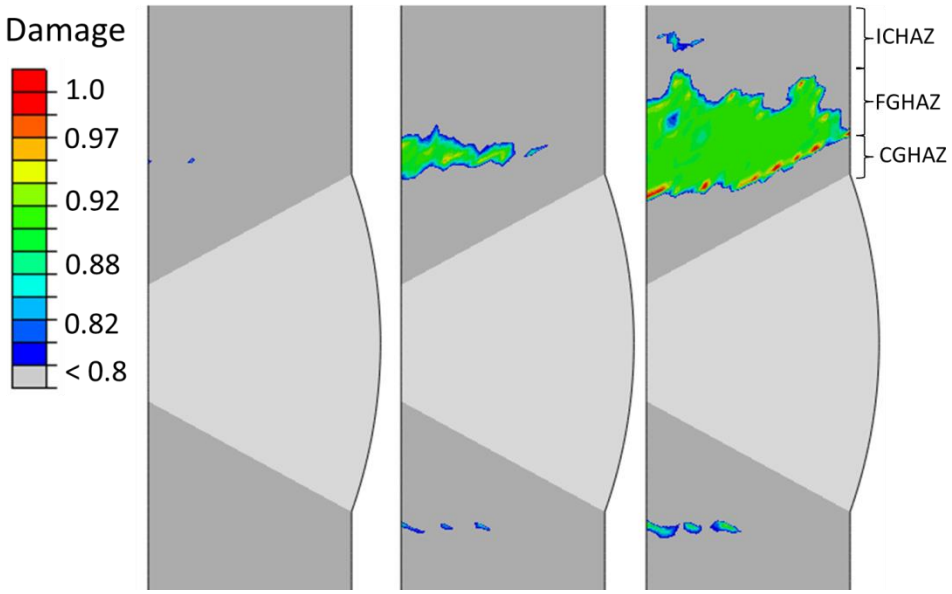

Fig. 20. Predicted damage evolution in the as-welded cross-weld 2% strain-range specimen after (a) 78 cycles, (b) 110 cycles and (c) 118 cycles. Note that WM microstructure evolution is not simulated.

Figure 21 shows that the predicted effect of increasing PWHT time is to increase fatigue life, following an essentially linear trend, although the effect of PWHT is predicted to saturate after approximately 15 minutes.

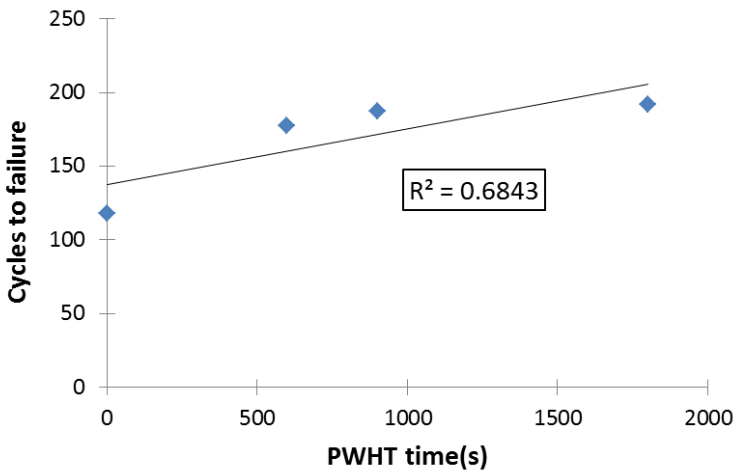

Fig. 21. The influence of PWHT time at 750°C on the number of cycles to failure for the given loading conditions.

Hardness testing is a common, non-destructive method for condition monitoring of material. Figure 22 shows that predicted CW life can be correlated with hardness gradient (see Fig. 18) across the HAZ as predicted by the model. The benefit of using the hardness gradient rather than discrete sample hardness values is the greater number of measurements which are therefore less likely to be affected by any anomalous measurements.

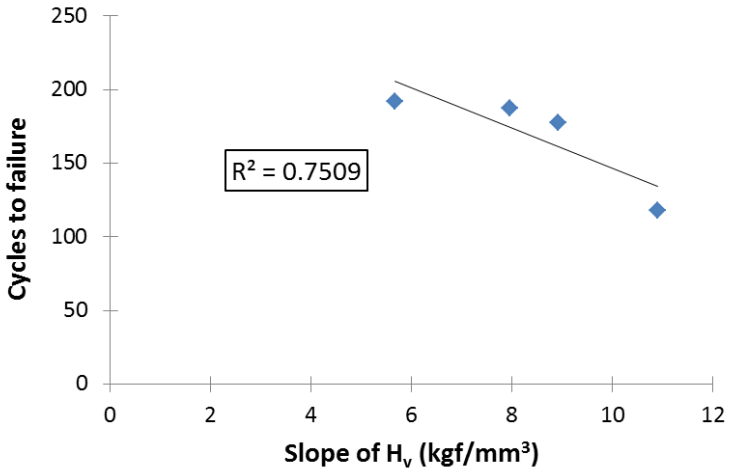

Fig. 22. The correlation between the slope of the Vickers hardness through the HAZ and the number of cycles to failure.

4 CONCLUSIONS

A through-process model for welding and post-weld thermo-mechanical tensile and cyclic response is presented for 9Cr ferritic-martensitic steel. The model incorporates empirically-based evolutions of hardness, solid-state phases, lath width and prior austenite grain size, and explicitly simulates the effects of process-induced thermal history and associated thermo-mechanical response on these variables and vice-versa. Some key conclusions are as follows:

- The model predicts the evolution of a welding-induced heat-affected zone which is qualitatively consistent with experimentally-observed trends in prior-austenite grain size, hardness, lath width and regions in which austenite transformation occurred at high temperature.
- The model predicts inter-critical and fine-grained heat-affected regions of untempered martensite, with associated lath refinement, localized hardening and reduced ductility for a given weld geometry.
- The model predicts the detrimental effects of welding on high temperature fatigue response, consistent with experimental observations.
- The beneficial effect of post-weld heat treatment on lath recovery (tempering) is also simulated, leading to an associated recovery in cyclic behavior and (low cycle) fatigue performance from the as-welded condition. A 10-minute PWHT at 750^{o}C increases predicted welded life by 50% for a 2% strain-range.
- The predicted number of cycles to failure is shown to correlate with predicted Vickers hardness gradient across the heat-affected zone.

5 ACKNOWLEDGEMENTS

This research is funded by Science Foundation Ireland grant number SFI/14/IA/2604. The authors would like to acknowledge the contributors to this research; NUI Galway, the Ryan Institute, General Electric (UK), ESB International, University of Limerick, Imperial College, London and Fraunhofer IWM, Freiburg.

REFERENCES

1. European Commission, *A policy framework for climate and energy in the period 2020 to 2030.* Communication from the commission to the European parliament, the council, the European economic and social committee and the committee of the regions, 2014.
2. Sauzay, M., Brillet, H., Monnet, I., Mottot, M., Barcelo, F., Fournier, B., Pineau, A., *Cyclically induced softening due to low-angle boundary annihilation in a martensitic steel.* Materials Science and Engineering A, 2005. **400-401**: p. 241-244.
3. Hurtado-Norena, C., Danón, C. A., Luppo, M. I.,Bruzzoni, P., *Evolution of Minor Phases in a P91 Steel Normalized and Tempered at Different Temperatures.* Procedia Materials Science, 2015. **8**: p. 1089-1098.
4. Ennis, P.J., Czyrska-Filemonowicz, A., *Recent Advances in Creep Resistant Steels for Power Plant Applications.* Operation Maintenance and Materials Issue, 2002. **1**(1).
5. Farragher, T.P., Scully, S., O'Dowd, N. P., Hyde, C. J., Leen, S. B., *High Temperature, low cycle fatigue characterisation of P91 weld and heat affected zone material.* Journal of Pressure Vessel Technology, 2014. **136**: p. 021403-1 - 021403-10.
6. Abe, F., Tabuchi, M., Tsukamoto, S., Shirane, T., *Microstructure evolutution in HAZ and suppression of Type IV fracture in advanced ferritic power plant steels.* International Journal of Pressure Vessels and Piping, 2010. **87**: p. 598-604.
7. Abe, F., Tabuchi, M., Kondo, M., Tsukamoto, S., *Suppression of Type IV fracture and improvement of creep strength of 9Cr steel welded joints by boron addition.* International Journal of Pressure Vessels and Piping, 2007. **84**: p. 44-52.
8. Mac Ardghail, P., Barrett, R. A., Harrison, N., Leen, S. B. *Towards a Through-Process model for welding of 9Cr steels*. in *10th International Conference on Trends in Welding Research, TWR 2016, & 9th International Welding Symposium of Japan Welding Society (9WS)*. 2016. Tokyo, Japan.
9. Mac Ardghail, P., Barrett, R. A., Harrison, N., Leen, S. B. *Predictions of ICHAZ thermo-mechanical response in GTAW process for 9Cr steels*. in *ASME 2017 Pressure Vessels and Piping Conference, PVP 2017*. 2017. Waikoloa, Hawaii, USA.
10. Yaghi, A.H., Hyde, T. H., Becker, A. A., Sun, W., *Finite element simulation of residual stresses induced by the dissimilar welding of a P92 steel pipe with weld metal IN625.* International Journal of Pressure Vessels and Piping, 2013. **111-112**: p. 173-186.
11. Touboul, M., Crepin, J., Rousselier, G., Latourte, F., Leclercq, S., *Identification of Local Viscoplastic Properties in P91 Welds from Full Field Measurements at Room Temperature and 625 ^{o}C.* Experimental Mechanics, 2013. **53**: p. 455-468.
12. Yaghi, A.H., Hyde, T. H., Becker, A. A., Williams, J. A., Sun, W., *Residual stress simulation in welded sections of P91 pipes.* Journal of Materials Processing Technology, 2005. **167**: p. 480-487.

13. Koistinen, D.P., Marburger, R.E, *A general equation prescribing the extent of the austenite-martensite transformation in pure iron-carbon alloys and plain carbon steels.* Acta Metallurgica, 1959. **7**(1): p. 59-60.
14. Vallourec & Mannesmann Tubes, *V & M Experience in T/P91 Tubes and Pipes*, in *International Workshop on Fabrication & Processing of Grade 91 Material, FAB 91*2011: Tiruchirappalli, India.
15. Cerjak, H., *The Role of Welding in the Power Generation Industry.* Proceedings of the International Conference Safety and Reliability of Welded Components, 2008: p. 17-27.
16. Francis, J.A., Bhadeshia, H. K. D. H., Withers, P. J., *Welding residual stresses in ferritic power plant steels.* Materials Science and Technology, 2007. **23**(9): p. 1009-1020.
17. Potirniche, G., Charit, I., Rink, K., Barlow, F., *Prediction and monitoring systems of creep-fracture behaviour of 9Cr-1Mo steels for reactor pressure vessels.* NEUP 2009 Project, 2013. **09-835**.
18. Milovic, L., Vuherer, T., Blacic, I., Vrhovac, M., Stankovic, M., *Microstructures and mechanical properties of creep resistant steel for application at elevated temperatures.* Materials and Design, 2013. **46**: p. 660-667.
19. Li, H., Lin. J., Dean, T. A., Wen, S. W., Bannister, A. C., *Modelling mechanical property recovery of a linepipe steel in annealing process.* International Journal of Plasticity, 2009. **25**: p. 1049-1065.
20. Barbadikar, D.R., Deshmukh, G. S., Maddi, L., Laha, K., Parameswaran, P., Ballal, A. R., Peshwe, D. R., Paretkar, R. K., Nandagopal, M., Mathew, M. D., *Effect of normalizing and tempering temperatures on microstrucutre and mechanical properties of P92 steel.* International Journal of Pressure Vessels and Piping, 2015. **132-133**: p. 97-105.
21. Wei, X., Asgari, S. A., Wang, J. T., Rolfe, B. F., Zhu, H. C., Hodgson, P. D., *Micromechanical modelling of bending under tension forming behaviour of dual phase steel 600.* Computational Materials Science, 2015. **108**: p. 72-79.
22. Li, M., Wang, L., Almer, J. D.,, *Dislocation evolution during tensile deformation in ferritic-martensitic steels revealed by high-energy X-rays.* Acta Materialia, 2014. **76**: p. 381-393.
23. Shankar, V., Sandhya, R., Mathew, M.D., *Creep-fatigue-oxidation interaction in Grade 91 steel weld joints for high temperature applications.* Materials Science and Engineering A, 2011. **528**: p. 8428-8437.
24. Barrett, R.A., O'Donoghue, P. E., Leen, S. B., *A dislocation-based model for high temperature cyclic viscoplasticity of 9-12Cr steels.* Computational Materials Science, 2014. **92**: p. 286-297.
25. Deng, D., Murakawa, H.,, *Numerical simulation of temperature field and residual stress in multi-pass welds in stainless steel pipe and comparison with experimental measurements.* Computational Materials Science, 2006. **37**: p. 269-277.
26. Dong, P., *Residual Stress Analyses of a Multi-Pass Girth Weld: 3-D Special Shell Versus Axisymmetric Models.* Journal of Pressure Vessel Technology, 2001. **123**: p. 207-213.
27. Abburi Venkata, K., Truman, C. E., Wimpory, R. C., Pirling, T.,, *Numerical simulation of a three-pass TIG welding using finite element method with validation from measurements.* International Journal of Pressure Vessels and Piping, 2017.
28. Goldack, J., Chakravarti, A., Bibby, M.,, *A new finite element model for welding heat sources.* Journal of Metallurgical Transactions B, 1984. **15**: p. 299-305.